



# One-step thermal synthesis of Ag-modified g-C<sub>3</sub>N<sub>4</sub>/N-doped TiO<sub>2</sub> hybrids with enhanced visible-light photocatalytic activity

Shanfu Sun<sup>1</sup>, Mingxuan Sun<sup>1,\*</sup>, Yuanyuan Kong<sup>2</sup>, Fangchao Liu<sup>1</sup>, Zhishui Yu<sup>1</sup>, Sambandam Anandan<sup>3</sup>, and Chun Chang<sup>4</sup>

<sup>1</sup>School of Materials Engineering, Shanghai University of Engineering Science, Shanghai 201620, China

<sup>2</sup>Shanghai Institute of Technical Physics, Chinese Academy of Sciences, Shanghai 200083, China

<sup>3</sup>Nanomaterials and Solar Energy Conversion Lab, Department of Chemistry, National Institute of Technology, Trichy 620015, India

<sup>4</sup>Department of Environmental Science and Engineering in College of Chemistry and Chemical Engineering, Bohai University, Jinzhou 121013, China

Received: 1 July 2016

Accepted: 14 September 2016

Published online:

20 September 2016

© Springer Science+Business Media New York 2016

## ABSTRACT

A series of silver nanoparticle-modified graphitic carbon nitride/N-doped TiO<sub>2</sub> hybrids (Ag/g-C<sub>3</sub>N<sub>4</sub>/N-TiO<sub>2</sub> or ACTs) were prepared by one-step in situ calcination process at 550 °C for 3 h in air atmosphere. The morphology, structure, and optical properties of ACTs with different Ag contents were characterized by X-ray diffraction, scanning electron microscopy, transmission electron microscopy, X-ray photoelectron spectroscopy, photoluminescence spectra, and UV–vis diffuse reflectance spectroscopy. Ag nanoparticles with grain size of about 5 nm are anchored on the surface of ACTs. In UV–vis absorption test, a red-shift of light absorption edge and more visible light absorption (compared to N-TiO<sub>2</sub> and g-C<sub>3</sub>N<sub>4</sub>/N-TiO<sub>2</sub>) are observed for ACTs. Moreover, the dependence of photocatalytic activity on Ag contents was investigated, and ACTs-3 presents the highest photocatalytic activity as the optimal Ag content under visible light irradiation. Remarkably enhanced UV–visible light photoelectrochemical response was also confirmed for ACTs compared with TiO<sub>2</sub>, N-TiO<sub>2</sub>, and g-C<sub>3</sub>N<sub>4</sub>/N-TiO<sub>2</sub>. Ag-decorated g-C<sub>3</sub>N<sub>4</sub>/N-TiO<sub>2</sub> composites result in enhanced light absorption capacity and improved transfer of charge carriers, which prominently contribute to the improvement of photoactivity. This work demonstrates that Ag/g-C<sub>3</sub>N<sub>4</sub>/N-TiO<sub>2</sub> is a promising photocatalytic material for organic pollutant degradation under visible light irradiation.

Address correspondence to E-mail: mingxuansun@sues.edu.cn; smxalan@163.com

## Introduction

TiO<sub>2</sub> has been widely investigated in various research fields including purification of wastewater or air pollutions [1, 2], hydrogen production [3, 4], and dye-sensitized solar cells [5, 6]. However, TiO<sub>2</sub> (with wide band gap of 3.0–3.2 eV) only activated efficiently under UV light irradiation [7], and hence lot of improvements are needed to extend the spectral response toward visible region [8, 9]. Among them, nitrogen doping has become one of the most studied focal points in the modification of TiO<sub>2</sub> [10, 11] and the resulted N-TiO<sub>2</sub> shows enhanced photocatalytic activities, because the doping of nitrogen impurities narrows the band gap and shifts the absorption edge of TiO<sub>2</sub> into the visible range [12, 13]. However, it has to be further altered a lot in order to promote its practical application.

Recently, graphitic carbon nitride (g-C<sub>3</sub>N<sub>4</sub>) has emerged as a promising candidate for photocatalysts due to its narrow band gap (~2.7 eV). In addition, the conjugated carbon and nitrogen structure of g-C<sub>3</sub>N<sub>4</sub>, which helps in coupling with a wide range of materials, makes it act as a co-catalyst to enhance the visible photocatalytic activity of other photocatalysts [14, 15]. Wang et al. [16] prepared N-TiO<sub>2</sub>/g-C<sub>3</sub>N<sub>4</sub> composites by a novel in situ microwave-assisted route, and such heterostructures exhibited better photodegradation performance of rhodamine B (RhB) and methyl blue (MB) compared with pristine N-TiO<sub>2</sub>. Han et al. [17] fabricated g-C<sub>3</sub>N<sub>4</sub> hybridized N-TiO<sub>2</sub> nanofibers composites by combined electro-spinning with modified heat-etching approach, and the resultant showed highly efficient photocatalytic activity on H<sub>2</sub> evolution and pollution degradation. Zhou et al. [18] synthesized a series of composites based on g-C<sub>3</sub>N<sub>4</sub> and N-TiO<sub>2</sub> by a pyrolysis process,

and such hybrids showed excellent photocatalytic performance and photostability in photoreduction of CO<sub>2</sub> to CO. In this concept, we also achieved higher photocatalytic activity for prepared g-C<sub>3</sub>N<sub>4</sub>/N-TiO<sub>2</sub> homogeneous mixture via solid phase calcination process at 550 °C for 3 h in air [17, 19].

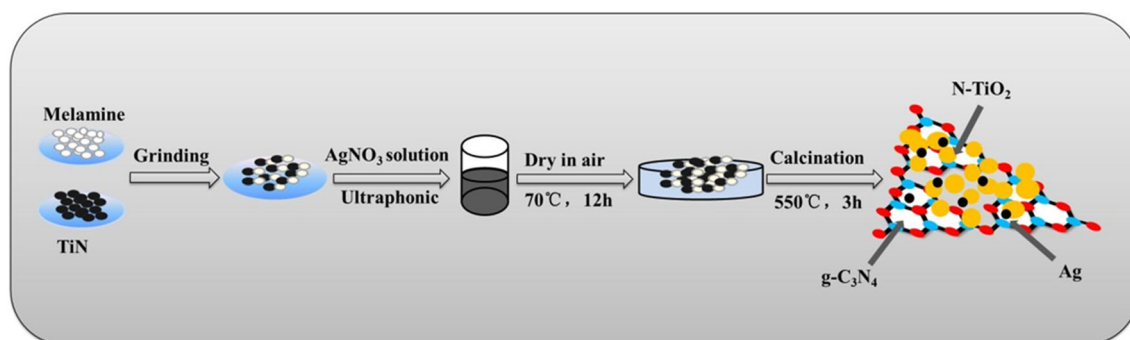
In general, Ag loading on any material can serve as trapping sites for electrons, thus improving the separation efficiency of electron–hole pairs [26], and hence it is a good alternative to improve the utilization efficiency of solar energy. Hence we tried here the modification of g-C<sub>3</sub>N<sub>4</sub>/N-TiO<sub>2</sub> homogeneous mixture with Ag loading to yield Ag/g-C<sub>3</sub>N<sub>4</sub>/N-TiO<sub>2</sub> nanocomposites via one-step in situ calcination process. The results indicated such composites showed a considerably enhanced activity of visible-light-induced photodegradation of MB.

## Experimental section

### Preparation of Ag/g-C<sub>3</sub>N<sub>4</sub>/N-TiO<sub>2</sub> hybrids

Melamine (C<sub>3</sub>H<sub>6</sub>N<sub>6</sub>, >99 %), TiN (99.9 %, 40 nm), and silver nitrate (AgNO<sub>3</sub>, 99.8 %) were purchased from Sinopharm Chemical Reagent Entrepreneur Corp., China. All chemicals for synthesis and analysis were commercially available and used without further treatments.

ACTs were synthesized by one-step in situ calcination process. The corresponding preparation process is illustrated schematically in Scheme 1. Briefly, 0.2 g of TiN and melamine with a mass ratio of 1:1 were vigorously grinded to obtain a homogeneous mixture and then dispersed in 20 ml of silver nitrate solution. The suspension ultrasonically vibrated for 1 h. After that, the precursors were dried at 70 °C for



**Scheme 1** Illustration of preparation of Ag/g-C<sub>3</sub>N<sub>4</sub>/N-TiO<sub>2</sub> nanocomposites by one-step in situ calcination process.

12 h to remove the solvent, followed by annealing at 550 °C for 3 h in air atmosphere. Thus, Ag/g-C<sub>3</sub>N<sub>4</sub>/N-TiO<sub>2</sub> nanocomposites were obtained with light gray color. The loading amount of Ag was adjusted by controlling the concentration of AgNO<sub>3</sub> solution (0, 0.003, 0.006, 0.012, and 0.024 M) in the process of preparing Ag/g-C<sub>3</sub>N<sub>4</sub>/N-TiO<sub>2</sub> nanocomposites, and the relevant products were denoted as ACTs-0, ACTs-1, ACTs-2, ACTs-3, and ACTs-4, respectively. Blank N-TiO<sub>2</sub> and g-C<sub>3</sub>N<sub>4</sub> were synthesized via calcination of TiN and melamine at 550 °C for 3 h in air, respectively.

### Characterizations

X-ray diffraction (XRD) was carried out on a PANalytical X' Pert X-ray diffractometer (Holland) with Cu-K $\alpha$  radiation at 40 kV and 40 mA. The morphologies of the samples were characterized by scanning electron microscopy (SEM, Model: JEOL JSM-7000F, Japan) and high-resolution transmission electron microscopy (HR-TEM, Model: FEI Tecnai F20, USA). The UV–vis diffuse reflectance spectra (UV–vis DRS) were recorded using a Shimadzu UV 3600 (Japan) spectrophotometer. The X-ray photoelectron spectroscopy (XPS) analysis was performed on a RBD upgraded PHI-5000 C ESCA system (PerkinElmer) with Al/MgK $\alpha$  as the radiation source. The photoluminescence (PL) spectra were obtained using an Edinburgh FLsp920 spectrophotometer at an excitation wavelength of 350 nm.

### Photocatalytic tests

The photocatalytic activities of the prepared photocatalysts were tested for the degradation of MB under visible light irradiation. Typically, 15 ml of MB solution (5 mg/L) and 7.5 mg of photocatalysts were taken in a 50 ml reactor and the suspension was agitated in darkness for 2 h to ensure adsorption/desorption equilibrium, prior to irradiation. Subsequently, photodegradation process was carried out under visible light irradiation. A spherical Xe lamp (CHF-XM-500 W, Beijing) equipped with cut filters ( $\lambda > 420$  nm) was used as the visible light source for photocatalysis. The light intensity of the lamp was 130 mW/cm<sup>2</sup>, which was measured by a light-intensity meter (FZ-A, Photoelectric Instrument Factory of Beijing Normal University). At given time intervals, 5 ml of the suspension was sampled and

centrifuged to remove the photocatalyst. Then, the concentration of MB was analyzed using a UV–vis spectroscopy (Shimadzu UV 1601-PC, Japan) in the wavelength range of 400–800 nm. The photodegradation results were reported as  $C/C_0$  and  $\ln(C_0/C)$ , where  $C_0$  and  $C$  were the pollutants concentration after adsorption and photocatalysis, respectively.

### Photoelectrochemical measurements

The photoelectrochemical performance was measured on a CHI 660E electrochemical workstation (Shanghai Chenhua Instruments, China) in a PEC cell with Pt foil as counter electrode and saturated calomel electrode (SCE) as reference electrode. 0.5 M Na<sub>2</sub>SO<sub>4</sub> aqueous solution was used as the electrolyte. The working electrodes prepared on a FTO glass plate were illuminated under 500 Xe lamp, and the light intensity was 160 mW/cm<sup>2</sup>. Electrochemical impedance spectra (EIS) were recorded in the frequency range from 0.01 Hz to 100 kHz. All measurements were carried out under ambient conditions at room temperature.

### Results and discussion

The crystal structures and phase of the obtained samples were characterized by XRD (Fig. 1). Figure 1a shows the XRD patterns of g-C<sub>3</sub>N<sub>4</sub>, N-TiO<sub>2</sub>, ACTs-0, and ACTs-3 samples. Pure g-C<sub>3</sub>N<sub>4</sub> exhibits two distinct peaks at 13.1° and 27.4°, which are indexed to (100) and (002) diffraction planes, respectively [20]. The diffraction peaks of N-TiO<sub>2</sub> observed at  $2\theta$  values of 25.4°, 27.5°, 37.8°, 48.0°, 53.9°, and 56.6° correspond to the (101), (110), (004), (200), (105), and (220) (JCPDS 03-065-5714; 03-065-0191) crystal planes of TiO<sub>2</sub>. Obviously, the as-prepared N-TiO<sub>2</sub> is composed of anatase and rutile phase. The rutile phase is determined to be 15 % according to the integrated intensities of anatase (101) and rutile (110) peaks. Scherrer's equation is applied to the anatase (101) planes, and the crystallite size is calculated to be around 30 nm for N-TiO<sub>2</sub>. Compared with XRD patterns of N-TiO<sub>2</sub>, ACTs-0 sample exhibits almost similar diffraction peaks but a stronger intensity at 27.4°, which may be attributed to the overlapping of (110) plane of TiO<sub>2</sub> and (002) plane of g-C<sub>3</sub>N<sub>4</sub>. Furthermore, strong additional diffraction peaks at 38.1°, 44.3°, 64.4°, and 77.4° can be observed for the ACTs-3

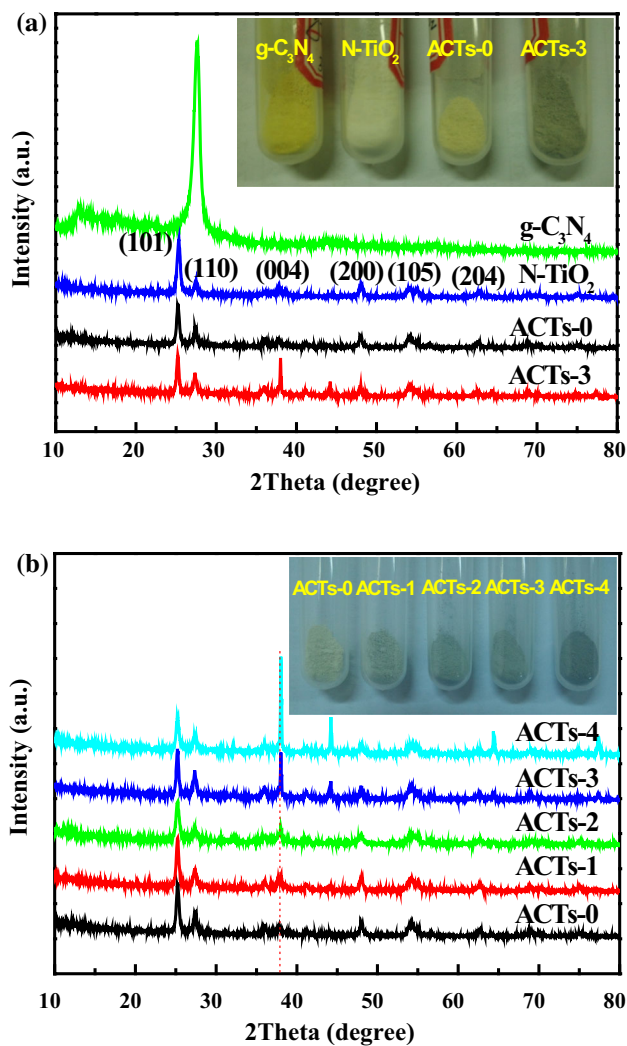


**Figure 1** XRD patterns of g-C<sub>3</sub>N<sub>4</sub>, N-TiO<sub>2</sub>, ACTs-0, and ACTs-3 samples (a), and ACTs-x composites with different Ag contents (b); The insets are the corresponding color evolution.

sample, which are assigned to (111), (200), (220), and (311) plane of Ag (JCPDS 01-087-0597). Figure 1b shows XRD patterns of ACTs-x ( $x = 1, 2, 3, 4$ ) composites with different Ag contents. The intensities of peak around 38.1° increase and the color of samples deepen gradually with the increase of Ag content in the composites. The XRD results imply the successful fabrication of Ag/g-C<sub>3</sub>N<sub>4</sub>/N-TiO<sub>2</sub> nanocomposites. In addition, the insets of Fig. 1a are the corresponding color evolution of g-C<sub>3</sub>N<sub>4</sub>, N-TiO<sub>2</sub>, ACTs-0, and ACTs-3, which is a visual evidence for the successful synthesis of the target resultants. The existence of Ag and g-C<sub>3</sub>N<sub>4</sub> in the composites could be further confirmed by XPS and TEM results, as described later.

The morphology and microstructure of the as-prepared samples were examined by FE-SEM

(Fig. 2a–c) and TEM (Fig. 3d–f). As shown in Fig. 2a–c, sphere nanoparticles with grain sizes around 50 nm are observed. It is difficult to tell the difference of morphologies between pure N-TiO<sub>2</sub>, ACTs-0, and ACTs-3. The TEM images provide a more clear observation. Figure 2d displays the HR-TEM images of ACTs-0 sample. The lattice fringes of 0.352 and 0.233 nm are ascribed to the (101) and (112) planes of anatase TiO<sub>2</sub> [21], respectively, while the value of 0.310 nm is attributed to the (110) planes of rutile [22]. This observation confirms the co-existence of anatase and rutile TiO<sub>2</sub>, which further corroborates the results of XRD. In addition, it is also clearly observed that g-C<sub>3</sub>N<sub>4</sub> shows stacked layer structure. Figure 2e, f presents the HR-TEM images of ACTs-3. As shown in Fig. 2e, it is clearly seen that Ag nanoparticles, loading on the surface of g-C<sub>3</sub>N<sub>4</sub>/N-TiO<sub>2</sub>, present spherical structure with an average diameter of 5 nm. Moreover, layered g-C<sub>3</sub>N<sub>4</sub>, characteristic lattice fringes of TiO<sub>2</sub>, and spherical Ag nanoparticles are observed for ACTs-3 in Fig. 2f, demonstrating the successful fabrication of Ag/g-C<sub>3</sub>N<sub>4</sub>/N-TiO<sub>2</sub>.

The surface composition and chemical states of the as-prepared sample (ACTs-3) were detected by XPS (Fig. 3a–f), and the binding energies analysis is corrected for specimen charging by referencing C 1 s to 284.6 eV. Figure 3a provides the general XPS for ACTs-3 sample over a large energy range at low resolution. It shows the presence of C 1 s, Ag 3d, N 1 s, Ti 2p, O 1 s, and Ti 2 s. Figure 3b shows the Ag 3d core-level XPS spectrum. Two individual peaks at around 368.1 and 374.0 eV are attributed to Ag 3d<sub>5/2</sub> and 3d<sub>3/2</sub>, respectively, indicating Ag particles exist in the form of zero-valence [28]. Figure 3c shows the Ti 2p core-level spectrum: the binding energies for Ti 2p<sub>3/2</sub> and Ti 2p<sub>1/2</sub> appear at 458.4 and 464.2 eV, respectively. According to earlier report [23], the Ti 2p<sub>3/2</sub> of pure TiO<sub>2</sub> should be located at the binding energy of 458.8 eV. Apparently, nitrogen doping results in a decrease of Ti 2p<sub>3/2</sub>-binding energy, suggesting a change in the electron density around the Ti atoms. This phenomenon can be ascribed to the lower electronegativity of N compared to O, partial electron transfer can occur from the N to the Ti [24]. Figure 3d shows that the O 1 s peaks center at the binding energies of 529.6 and 531.4 eV. The peak at 529.6 eV is associated with the Ti–O bond in N-TiO<sub>2</sub> [25], while the other O 1 s peak at 531.4 eV is probably related to the hydroxyl groups (H–O bonds) on the surface of ACTs-3 or the presence of Ti–O–N bonds as

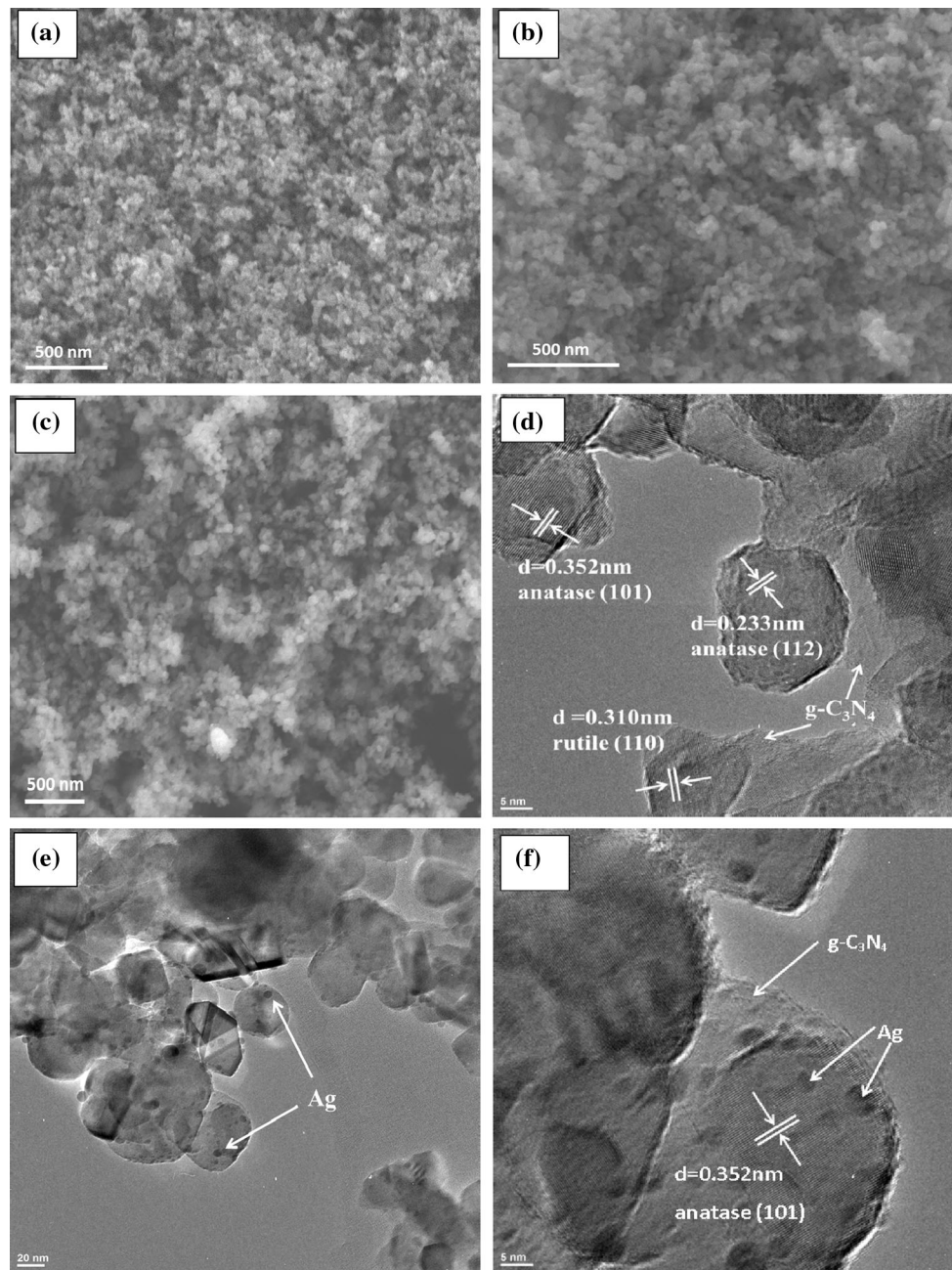


**Figure 2** SEM images of N-TiO<sub>2</sub> (a), ACTs-0 (b), ACTs-3 (c); HR-TEM images of ACTs-0 (d), and ACTs-3 (e, f) samples.

in previous reports [14, 26]. Two peaks are observed from the C 1 s core-level spectrum shown in Fig. 3e. The peak at 284.6 eV is ascribed to the carbon contamination, and the peak at 288.2 eV is assigned to the N-C=N group in graphitic carbon nitride [27]. As shown in Fig. 3f, the N 1 s core-level spectrum can be fitted with three peaks. The peak centered at 398.8 eV is attributed to the  $sp^2$ -hybridized nitrogen (C=N-C) group of g-C<sub>3</sub>N<sub>4</sub> [28]. And the other two peaks located

at 399.7 and 401.2 eV are derived from N-TiO<sub>2</sub>, which indicates N atoms may locate at the interstitial sites of the TiO<sub>2</sub> lattice and form Ti-O-N or Ti-N-O [23]. Based on the above XPS analysis, we can draw the conclusion that the Ag/g-C<sub>3</sub>N<sub>4</sub>/N-TiO<sub>2</sub> composites were successfully obtained.

UV-vis absorption spectra (a) and UV-vis reflectance spectra (b) of the as-prepared samples are shown in Fig. 4. All the ACTs-*x* (*x* = 1, 2, 3, 4)

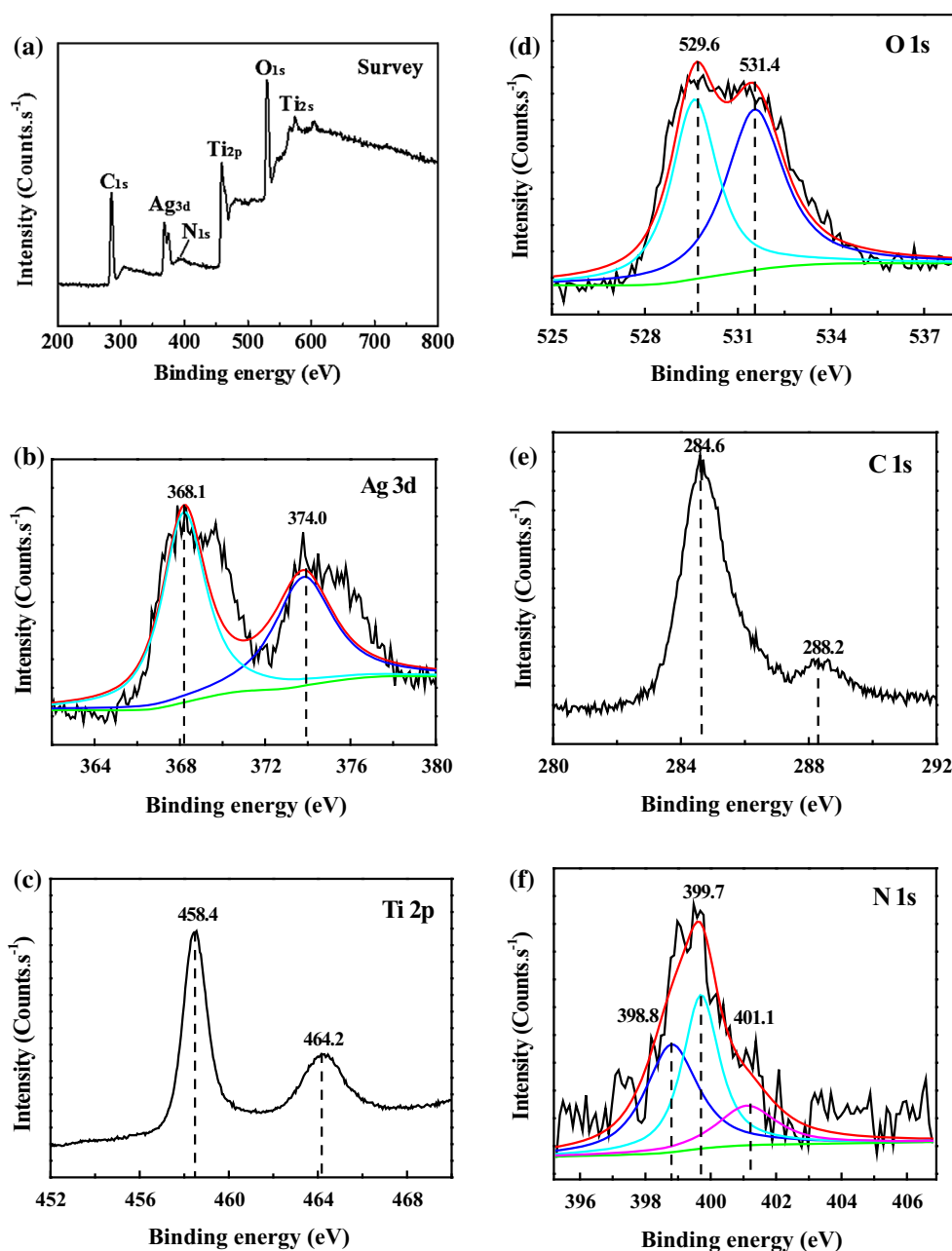
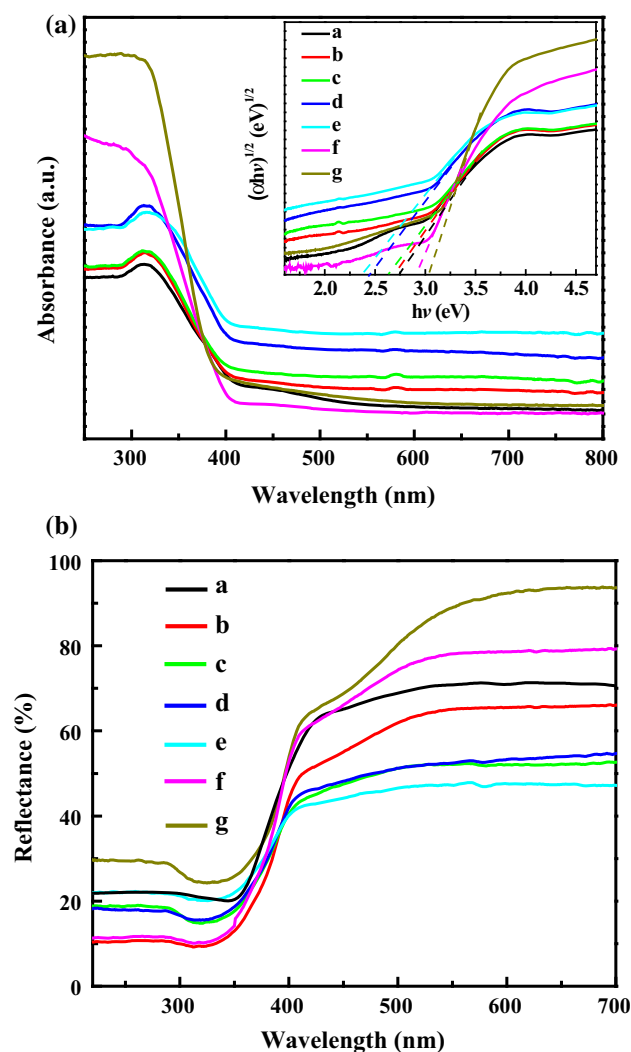


**Figure 3** XPS general spectrum (a) and the core-level XPS of Ag 3d (b), Ti 2p (c), O 1 s (d), C 1 s (e) and N 1 s (f) of ACTs-3 composite.

samples show strong absorption in visible region, and the visible light absorption capacity gradually enhances with the increase of Ag loading content. The band gaps of ACTs-0, ACTs-1, ACTs-2, ACTs-3, ACTs-4, N-TiO<sub>2</sub>, and P25 are estimated to be about 2.75, 2.70, 2.65, 2.40, 2.30, 2.90, and 3.10 eV, according to the absorption edges at about 450, 459, 468, 516, 540, 428, and 400 nm, respectively. As shown in Fig. 4b, UV–vis diffuse reflectance spectra reveal that the ACTs-*x* (*x* = 1, 2, 3, 4) samples exhibit a wider

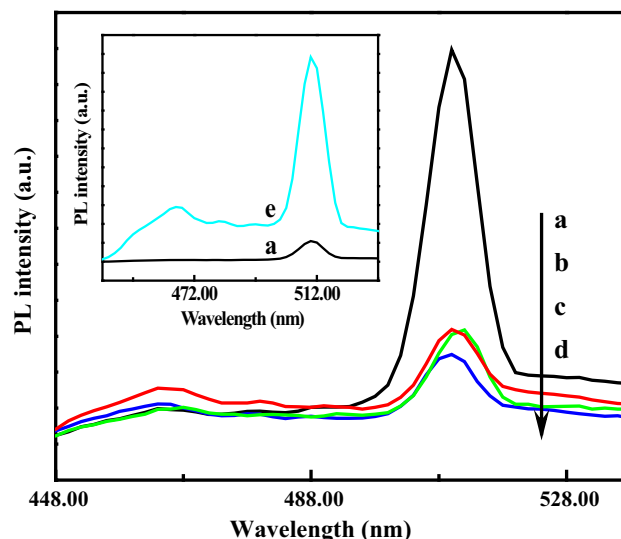
and stronger absorption of visible light than that of bare ACTs-0, N-TiO<sub>2</sub>, and P25 samples, which is consistent with the absorption spectra results. These results indicate that the red-shift of absorption edge and narrower band gap are achieved for TiO<sub>2</sub> with modification of Ag loading, g-C<sub>3</sub>N<sub>4</sub> coupling, and N doping, which is beneficial to the visible-light-driven photocatalytic performance.

Figure 5 shows the PL spectra of ACTs-0, ACTs-1, ACTs-2, ACTs-3, and ACTs-4 samples. All the



**Figure 4** UV–vis absorption spectra (a) and UV-vis reflectance spectra (b) of ACTs (a), ACTs-1 (b), ACTs-2 (c), ACTs-3 (d), ACTs-4 (e), N-TiO<sub>2</sub> (f), and P25 (g) samples; The inset is the estimated band gap by Kubelka–Munk function.

samples show two emission peaks at 460 and 510 nm. The emission at 510 nm with band gap energy of 2.44 eV is attributed to the transition from isolated N 2*p* level to the conduction band of TiO<sub>2</sub> [29]. The emission at 460 nm can be assigned to the g-C<sub>3</sub>N<sub>4</sub> photoluminescence [24]. It is also observed that the intensity of the luminescence peaks becomes weaker as bits of Ag deposited on g-C<sub>3</sub>N<sub>4</sub>/N-TiO<sub>2</sub> sample (ACT-1, ACT-2, and ACT-3). This can be ascribed to efficient interfacial electron transfer from the conduction band of ACTs-0 to the Ag species, which act as electron sinks and suppress the recombination of photoinduced carriers [30]. The lower intensity of PL peak implies that the fewer recombinations of



**Figure 5** PL spectra of ACTs-0 (a), ACTs-1 (b), ACTs-2 (c), ACTs-3 (d), and ACTs-4 (e) samples.

electron and hole pairs occur. However, the PL intensity of ACT-4 is obviously higher than ACTs-0 (See inset of Fig. 5), which indicates that excess amount of Ag on g-C<sub>3</sub>N<sub>4</sub>/N-TiO<sub>2</sub> surface will act as the recombination center of electrons and holes, leading to the low quantum efficiency.

The photocatalytic activity of ACTs was investigated using the model pollutant MB in aqueous solution. As shown in Fig. 6, the photodegradation of MB in the absence of photocatalyst is negligible. It is found that ACTs-3 sample is optimum to achieve the highest photodegradation efficiency of MB. The photodegradation rate of MB generally follows pseudo-first-order kinetic process, which can be expressed by the equation  $-\ln(C/C_0) = k_x t$ , where  $k_x$  is the pseudo-first-order rate constant. The calculated reaction rate constants of MB degradation under visible light irradiation are 0.0094, 0.0137, 0.0163, 0.0201, 0.0152, 0.0070, and 0.0036 min<sup>-1</sup> for ACTs-0, ACTs-1, ACTs-2, ACTs-3, ACTs-4, N-TiO<sub>2</sub>, and P25 samples, respectively (See inset of Fig. 6b). It is concluded that the photocatalytic activity of g-C<sub>3</sub>N<sub>4</sub>/N-TiO<sub>2</sub> can be enhanced by the loading of appropriate Ag content. The sample of ACTs-3 presents the highest reaction rate constant, which is 2.1 times higher than that of pure ACTs-0 sample. Excess amount of Ag is unfavorable for the photocatalytic process. The reaction rate constant for ACTs-4 is even smaller than that of ACTs-2 sample. There are two main reasons for the effect of Ag loading content on the photocatalytic activity of ACTs sample. On the

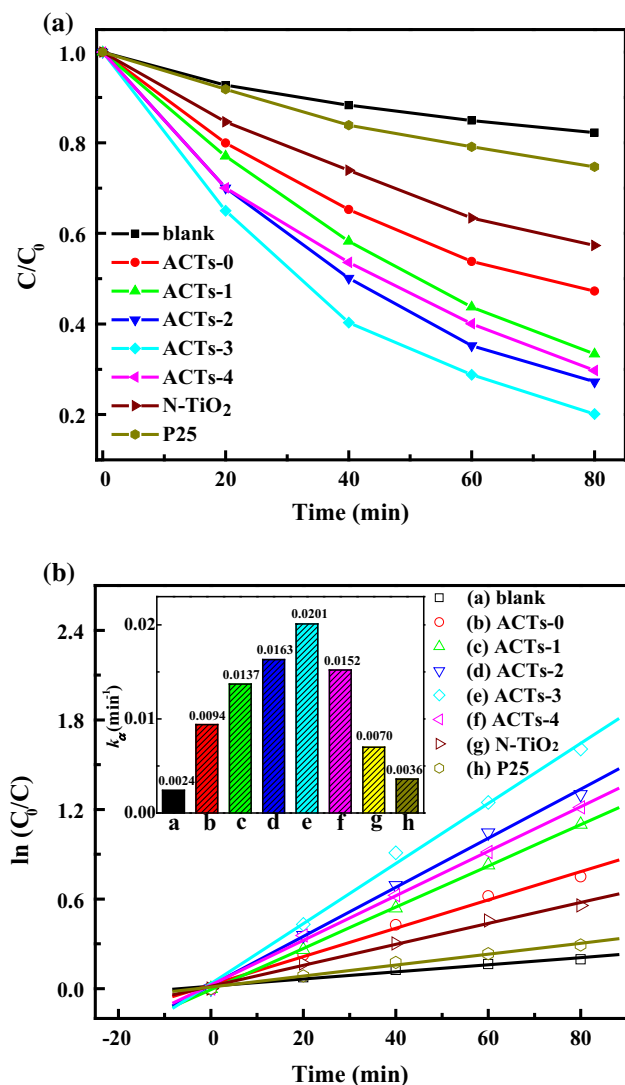


**Figure 6** Photocatalytic degradation of MB over the samples of P25, N-TiO<sub>2</sub>, and ACTs- $x$  ( $x = 0, 1, 2, 3, 4$ ) with different weight additions of Ag (a), pseudo-first-order kinetic plots (b) and inset is the comparison of rate constant.

one hand, excess amount of Ag loading on the surface of catalyst may influence the absorption of visible light, thus decrease the quantum efficiency, leading to lower concentration of photoinduced charge carrier [31]. On the other hand, excess amount of Ag species can act as recombination center of photogenerated electrons and holes, decreasing the separation efficiency of charge carriers [32].

The improved separation of photogenerated electron-hole pairs and prolonged lifetime of carriers can be demonstrated by the photoelectrochemical investigation (Fig. 7). It is observed that the photocurrent densities of P25, N-TiO<sub>2</sub>, ACTs-0, and ACTs-3

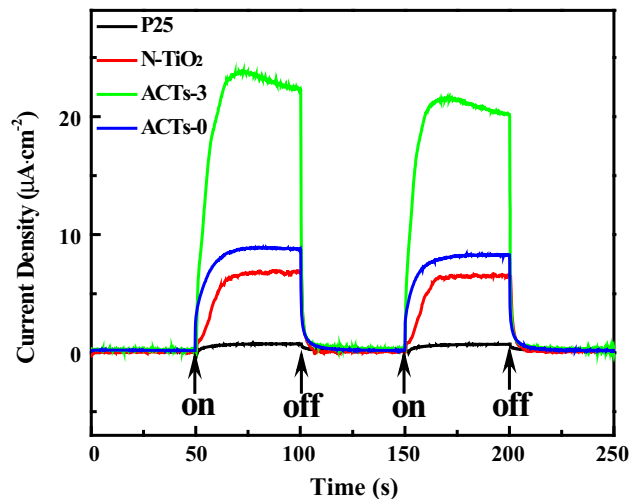


**Figure 7** Transient photocurrent response of P25, N-TiO<sub>2</sub>, ACTs-0, and ACTs-3 samples in 0.5 M Na<sub>2</sub>SO<sub>4</sub> aqueous solution without bias versus SCE.

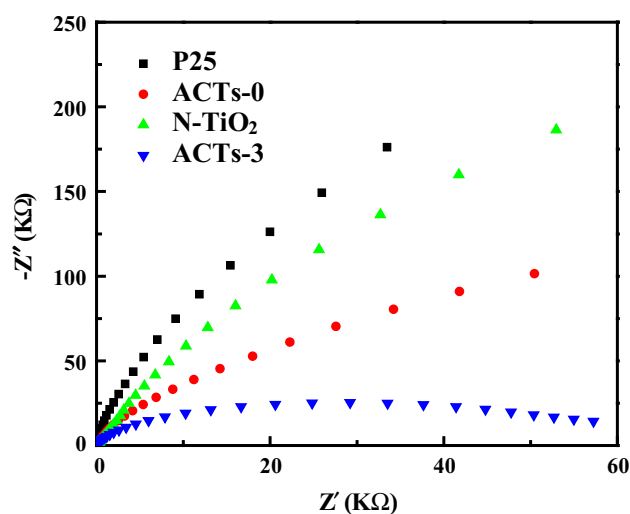
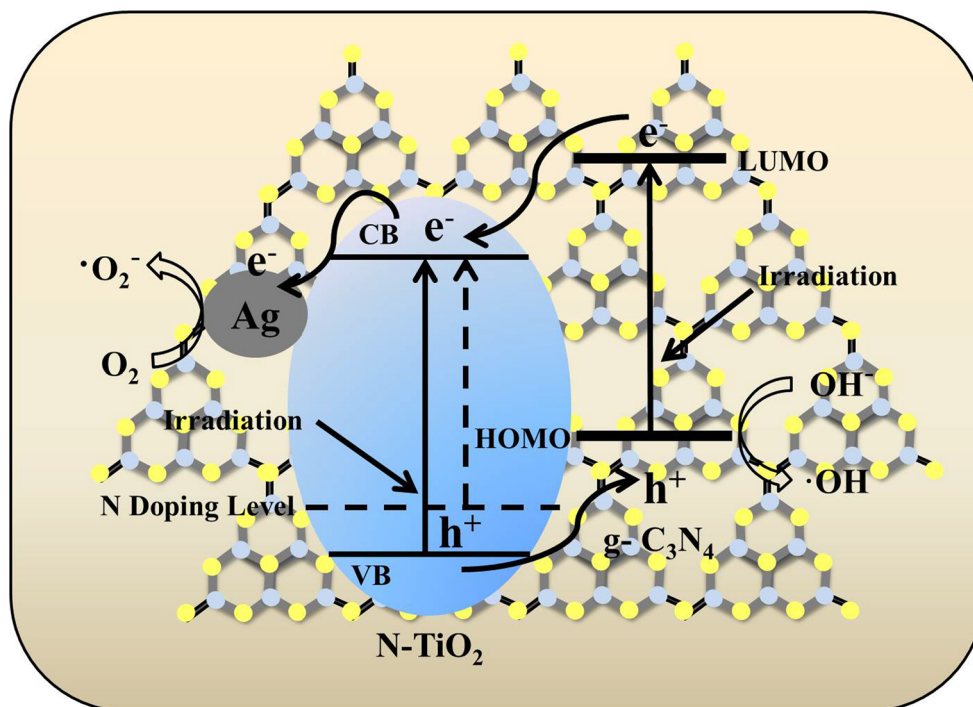


**Figure 8** EIS Nyquist plots of P25, N-TiO<sub>2</sub>, ACTs-0, and ACTs-3 samples electrodes in 0.5 M Na<sub>2</sub>SO<sub>4</sub> aqueous solution under dark condition.

samples are 0.74, 6.89, 8.83, and 23.8  $\mu\text{A}\cdot\text{cm}^{-2}$ , respectively. The photocurrent density of ACTs-3 sample is about 3 times more than that of the ACTs-0 electrode, confirming that longer life span is achieved with the introduction of Ag into g-C<sub>3</sub>N<sub>4</sub>/N-TiO<sub>2</sub> composites. This result is consistent with the PL analysis. The advantage of Ag loading on the surface of ACTs can be further confirmed by the electrochemical impedance spectra (EIS) results, as displayed in Fig. 8. It is observed that the semicircle diameter in Nyquist plots for ACTs-3 electrodes obviously decreased as compared to that of ACTs-0,



**Scheme 2** Schematic diagram of the proposed mechanism for the separation and transfer of photogenerated charges in Ag/g-C<sub>3</sub>N<sub>4</sub>/N-TiO<sub>2</sub> nanocomposites.



N-TiO<sub>2</sub>, and P25 samples, indicating a faster charge-carrier transfer rate in the Ag/g-C<sub>3</sub>N<sub>4</sub>/N-TiO<sub>2</sub> nanocomposite [33].

On the basis of the above results, a possible mechanism of visible light photocatalytic degradation of pollutants over the Ag/g-C<sub>3</sub>N<sub>4</sub>/N-TiO<sub>2</sub> is illustrated in Scheme 2. The conduction band (CB) and valence band (VB) potentials of TiO<sub>2</sub> are at  $-0.29$  and  $+2.91$  eV, while they are estimated to be  $-1.12$  and  $+1.57$  eV for g-C<sub>3</sub>N<sub>4</sub> [34], respectively. The N doping can efficiently enhance the visible light absorption of TiO<sub>2</sub>. Electrons are easily excited from the N impurity energy level to the conduction band of TiO<sub>2</sub> under visible light irradiation. In addition, g-C<sub>3</sub>N<sub>4</sub> can also activate under visible light irradiation. Due to the matching of the band structure between g-C<sub>3</sub>N<sub>4</sub> and N-TiO<sub>2</sub>, the photogenerated electrons from the CB of g-C<sub>3</sub>N<sub>4</sub> readily inject into the CB of N-TiO<sub>2</sub>, and the holes from the VB of N-TiO<sub>2</sub> can transfer to the VB of g-C<sub>3</sub>N<sub>4</sub>. Therefore, the recombination activity of photogenerated electrons and holes is suppressed, leaving more holes in the VB of g-C<sub>3</sub>N<sub>4</sub> and more electrons in the CB of N-TiO<sub>2</sub>. Subsequently, the electrons can accumulate on the Ag nanoparticles loaded on the surface of g-C<sub>3</sub>N<sub>4</sub>/N-TiO<sub>2</sub> which reduce the adsorbed O<sub>2</sub> rapidly to superoxide anion radicals ( $\cdot\text{O}_2^-$ ). Simultaneously, the photogenerated holes in the VB of g-C<sub>3</sub>N<sub>4</sub> react with

OH<sup>-</sup> to form  $\cdot\text{OH}$ . The highly active species  $\cdot\text{O}_2^-$  and  $\cdot\text{OH}$  are responsible for the degradation of MB.

## Conclusion

In this paper, a series of composites composed of Ag, g-C<sub>3</sub>N<sub>4</sub>, and N-TiO<sub>2</sub> were successfully prepared by a facile in situ calcination process, which are confirmed by characterizations including XRD, TEM, and XPS. The loading amount of Ag can be adjusted by controlling the concentration of AgNO<sub>3</sub> solution in the synthesis process. Enhanced visible light absorption and improved visible-light-induced photocatalytic performance were demonstrated for ACTs for photodegradation of methylene blue. The highest photocatalytic performance is observed for ACTs-3, which is about 2.1, 2.9, and 5.6 times larger than that of bare ACTs-0, N-TiO<sub>2</sub>, and P25, respectively. The positive effects of Ag loading, g-C<sub>3</sub>N<sub>4</sub> coupling, and N doping on TiO<sub>2</sub> are also confirmed by the photoelectrochemical measurements. The enhanced photoactivity of Ag/g-C<sub>3</sub>N<sub>4</sub>/N-TiO<sub>2</sub> is related to the effective separation of electro-hole pairs and an enhanced absorption of visible light, due to the synergistic interactions of TiO<sub>2</sub>, Ag, and N dopant in the as-prepared composites. This work promotes the

application of Ag/g-C<sub>3</sub>N<sub>4</sub>/N-TiO<sub>2</sub> in solar energy conversion and environmental remediation.

## Acknowledgements

This work was financially supported by Innovation Program of Shanghai Municipal Education Commission (15ZZ092), Training Program for Young Teachers in Shanghai Colleges and Universities (ZZgcd14010), Startup Foundation of Shanghai University of Engineering Science (NO. XiaoQi 2014-22), and National Natural Science Foundation of China (No. 51375294 and 51508026).

## References

- Sun MX, Li WB, Sun SF et al (2014) One-step in situ synthesis of graphene-TiO<sub>2</sub> nanorod hybrid composites with enhanced photocatalytic activity. *Mater Res Bull* 61:280–286
- Sun MX, Fang YL, Wang Y et al (2015) Synthesis of Cu<sub>2</sub>O/graphene/rutile TiO<sub>2</sub> nanorod ternary composites with enhanced photocatalytic activity. *J Alloy Compd* 650:520–527
- Xiang QJ, Yu JG, Jaroniec M (2012) Synergetic effect of MoS<sub>2</sub> and graphene as cocatalysts for enhanced photocatalytic H<sub>2</sub> production activity of TiO<sub>2</sub> nanoparticles. *J Am Chem Soc* 134:6575–6578
- Zhang XY, Sun YJ, Cui XL et al (2012) A green and facile synthesis of TiO<sub>2</sub>/graphene nanocomposites and their photocatalytic activity for hydrogen evolution. *Int J Hydrogen Energ* 37:811–815
- Zhu K, Neale NR, Miedaner A et al (2007) Enhanced charge-collection efficiencies and light scattering in dye-sensitized solar cells using oriented TiO<sub>2</sub> nanotubes arrays. *Nano Lett* 7:69–74
- Sun MX, Cui XL (2013) Needle-shaped 3D dye-sensitized solar cells using anodized Ti wire and Pt nanoparticle/carbon fiber electrodes. *J Power Sources* 223:74–78
- Zhu J, Yang D, Geng J et al (2008) Synthesis and characterization of bamboo-like CdS/TiO<sub>2</sub> nanotubes composites with enhanced visible-light photocatalytic activity. *J Nanopart Res* 10:729–736
- Shanmugasundaram S, Horst K (2003) Daylight photocatalysis by carbon-modified titanium dioxide. *Angew Chem Int Edit* 42:4908–4911
- Yu JX, Liu SW, Xiu ZL et al (2009) Synthesis of sulfur-doped TiO<sub>2</sub> by solvothermal method and its visible-light photocatalytic activity. *J Alloy Compd* 471:23–25
- Asahi R, Morikawa T, Ohwaki T et al (2001) Visible-light photocatalysis in nitrogen-doped titanium oxides. *Science* 293:269–271
- Valentin CD, Finazzi E, Pacchioni G et al (2007) N-doped TiO<sub>2</sub>: theory and experiment. *Chem Phys* 339:44–56
- Sun MX, Song P, Li J et al (2013) Preparation, characterization and applications of novel carbon and nitrogen codoped TiO<sub>2</sub> nanoparticles from annealing TiN under CO atmosphere. *Mater Res Bull* 48:4271–4276
- Sun SF, Sun MX, Fang YL et al (2016) One-step in situ calcination synthesis of g-C<sub>3</sub>N<sub>4</sub>/N-TiO<sub>2</sub> hybrids with enhanced photoactivity. *RSC Adv* 6:13063–13071
- Wang XC, Blechert S, Antonietti M (2012) Polymeric graphitic carbon nitride for heterogeneous photocatalysis. *Acc Catal* 2:1596–1606
- Wang Y, Wang XC, Antonietti M (2012) Polymeric graphitic carbon nitride as a heterogeneous organocatalyst: from photochemistry to multipurpose catalysis to sustainable chemistry. *Angew Chem Int Edit* 51:68–89
- Wang XJ, Yang WY, Li FT et al (2013) In situ microwave-assisted synthesis of porous N-TiO<sub>2</sub>/g-C<sub>3</sub>N<sub>4</sub> heterojunctions with enhanced visible-light photocatalytic properties. *Ind Eng Chem Res* 52:17140–17150
- Han C, Wang YD, Lei YP et al (2015) In situ synthesis of graphitic-C<sub>3</sub>N<sub>4</sub> nanosheet hybridized N-doped TiO<sub>2</sub> nanofibers for efficient photocatalytic H<sub>2</sub> production and degradation. *J Mater Res* 8:1199–1209
- Zhou S, Liu Y, Li JM et al (2014) Facile in situ synthesis of graphitic carbon nitride (g-C<sub>3</sub>N<sub>4</sub>)-N-TiO<sub>2</sub> heterojunction as an efficient photocatalyst for the selective photoreduction of CO<sub>2</sub> to CO. *Appl Catal B* 158:20–29
- Sun MX, Fang YL, Sun SF et al (2016) Surface co-modification of TiO<sub>2</sub> with N doping and Ag loading for enhanced visible-light photoactivity. *RSC Adv* 6:12272–12279
- Ge L, Han CC, Liu J (2011) Novel visible light-induced g-C<sub>3</sub>N<sub>4</sub>/Bi<sub>2</sub>WO<sub>6</sub> composite photocatalysts for efficient degradation of methyl orange. *Appl Catal B* 108:100–107
- Liang YY, Wang HL, Casalongue HS et al (2010) TiO<sub>2</sub> nanocrystals grown on graphene as advanced photocatalytic hybrid materials. *Nano Res* 3:701–705
- Ramchiary A, Samdarshi SK (2015) Hydrogenation based disorder-engineered visible active N-doped mixed phase titania. *Sol Energ Mat Sol C* 134:381–388
- Wang HQ, Yan JP, Chang WF et al (2009) Practical synthesis of aromatic amines by photocatalytic reduction of aromatic nitro compounds on nanoparticles N-doped TiO<sub>2</sub>. *Catal Commun* 10:989–994
- Parida KM, Pany S, Naik B (2013) Green synthesis of fibrous hierarchical meso-macroporous N doped TiO<sub>2</sub> nanophotocatalyst with enhanced photocatalytic H<sub>2</sub> production. *Int J Hydrogen Energ* 38:3545–3553
- Górska P, Zaleska A, Kowalska E et al (2008) TiO<sub>2</sub> photoactivity in Vis and UV light: the influence of calcination

- temperature and surface properties. *Appl Catal B* 84:440–447
- [26] Liu L, Ma D, Zheng H et al (2008) Synthesis and characterization of microporous carbon nitride. *Micropor Mesopor Mat* 110:216–222
- [27] Wang SP, Li CJ, Wang T et al (2014) Controllable synthesis of nanotube-type graphitic C<sub>3</sub>N<sub>4</sub> and their visible-light photocatalytic and fluorescent properties. *J Mater Chem A* 2:2885–2890
- [28] Yan SC, Li ZS, Zou ZG (2010) Photodegradation of rhodamine B and methyl orange over boron-doped g-C<sub>3</sub>N<sub>4</sub> under visible light irradiation. *Langmuir* 26: 3894–3901
- [29] Nakamura R, Tanaka T, Nakato Y (2004) Mechanism for visible light responses in anodic photocurrents at N-Doped TiO<sub>2</sub> film electrodes. *J Phys Chem B* 108:10617–10620
- [30] Georgekutty R, Seery MK, Pillai SC (2008) A highly efficient Ag-ZnO photocatalyst: synthesis, properties, and mechanism. *J Phys Chem C* 112:13563–13570
- [31] Lu WW, Liu GS, Gao SY et al (2008) Tyrosine-assisted preparation of Ag/ZnO nanocomposites with enhanced photocatalytic performance and synergistic antibacterial activities. *Nanotechnology* 19:82–85
- [32] Ren L, Zeng YP, Jiang D (2009) Preparation, characterization and photocatalytic activities of Ag-deposited porous TiO<sub>2</sub> sheets. *Catal Commun* 10:645–649
- [33] Pan XY, Xu YJ (2015) Graphene-templated bottom-up fabrication of ultralarge binary CdS-TiO<sub>2</sub> nanosheets for photocatalytic selective reduction. *J Phys Chem C* 119:7184–7194
- [34] Wang X, Maeda K, Thomas A et al (2008) A metal-free polymeric photocatalyst for hydrogen production from water under visible light. *Nat Mater* 8:76–80